Neutron tomography developments and applications

W.J. Richards[a], M.R. Gibbons[b], K.C. Shields[c]

[a] University of California, Davis McClellan Nuclear Radiation Center
[b] McClellan Nuclear Radiation Center, McClellan, California
[c] Science Applications International Corporation, McClellan, California

Abstract

Neutron radiography has been in use as a nondestructive testing technique for the past fifty years. The neutrons' unique ability to image certain elements and isotopes that are either completely undetectable or poorly detected by other NDI methods makes neutron radiography an important tool for the NDI community. Neutron radiography like other imaging techniques takes a number of different forms (i.e., film, radioscopic, transfer methods, tomography, etc.)

This paper will describe the neutron tomography system developed at the University of California, Davis McClellan Nuclear Radiation Center (UC Davis/MNRC), and the applications for both research and commercial uses.

The neutron radiography system at the UC Davis/MNRC has been under development for four years. The initial system was developed to find very low concentrations of hydrogen (i.e., < 200 ppm). In order to achieve these low detection levels, it was necessary to perform both pre- and post-processing of the tomographs.

The pre-processing steps include corrections for spatial resolution and random noise effects. Images are corrected for systematic noise errors and beam hardening. From these data the attenuation coefficient is calculated.

The post-processing steps include alignment of the collected images, determining the center of mass, and, finally, using the filtered back-projection routine from the Donner Algorithms Library to obtain the final images.

Since its initial development, the tomography system has been used very successfully to find low levels of hydrogen in a metal matrix. Further uses of the system have been to verify the exact placement, in three dimensions, of "O-rings" in large metal valve bodies, and to map the location and extent of veins in porous and high-density rocks of various different kinds.

These examples show that neutron tomography is becoming a needed inspection technique for the 21st century.

Introduction

Neutron radiography has already proven itself as a reliable method for the detection of hydrogenous substances, such as moisture and corrosion, in aircraft components[1]. Internal properties of objects are distinguished by differences in the attenuation coefficient of different materials. The advantage with neutrons is that some low atomic number nuclei, in particular, hydrogen, have higher interaction cross sections than the surrounding metal. Traditional radiography has limits since it only provides information on the total attenuation integrated over the path of the radiation through the material. The actual distribution of materials across that path is not known precisely.

The University of California, Davis McClellan Nuclear Radiation Center (UCD/MNRC)[2,3] has several programs for the use of neutron tomography as a nondestructive inspection (NDI) technique. Among these is quantitative hydrogen concentration data for metal castings. The hydrogen concentration can be used as an indicator for the loss of mechanical properties due to embrittlement, which can occur in metals after exposure to hydrogen.[4,5] The need for a NDI technique led to the investigation of neutron tomography.[6,7] The goal for this tomography system is to provide accurate hydrogen concentration data from several thousand down to 200 ppm by weight of hydrogen in titanium alloys with an object testing rate of three per hour. Objects such as aircraft engine compressor blades must be accommodated precluding the use of simple radiography that might be appropriate for a flat plate of metal.

The requirements for a system that achieves the above goal result in certain characteristics. The order of magnitude variation in spatial dimensions of the blades coupled with the rapid production rate favor a large neutron beam with a relatively high flux. The system must also be able to perform with a minimum number of tomographic projections to save time while maintaining a spatial resolution sufficient to characterize an object of 0.5 mm size. The requirement to detect the distribution of low hydrogen concentrations resulted, as mentioned previously, in the choice of tomography over radiography. In addition, errors and artifacts in the projections and reconstructions must be minimized to increase the signal to noise ratio for the calculated attenuation coefficients.

This paper describes the tomography system, the radiograph preprocessing, and the reconstruction postprocessing implemented to meet the system requirements for determining very low levels of hydrogen concentration in a titanium matrix. Reconstructions of various samples are shown to validate the techniques. The resulting neutron tomography system is applicable to a wide range of NDI tasks, from metal valve inspection to geologic sample investigation.

1. Tomography System.

The tomography system consists of a neutron source, an object turntable, a scintillator screen, a mirror, a cooled CCD camera, and computer support[8] (Figure 1). The neutron source is a 2 MW TRIGA thermal reactor. The neutron beam is approximately 35 cm in diameter at the scintillation screen with an L/D of 140. The thermal neutron flux at 2 MW

reactor power is 1.2·E07 n/cm^2·s at the film plane with a gold cadmium ratio of 3. The object turntable is fixed to a specimen positioner that can place it at different positions and orientations. Normally the turntable is centered approximately 10 cm in front of the scintillator screen. The neutrons are detected with a Li^{6}F-ZnS-Cu scintillator NE426 screen that uses ^{6}Li as the neutron absorber[9]. Given the decrease in the ^{6}Li absorption cross section with increasing energy, most of the neutrons detected are in the thermal region of the energy spectrum. The exposure time increases by a factor of 10 when a cadmium strip is placed in the neutron beam. The screen light output is 1.7·E05 photons per neutron with an absolute scintillation efficiency of 9% and resolution limits of less than 100 µm.[9,10]

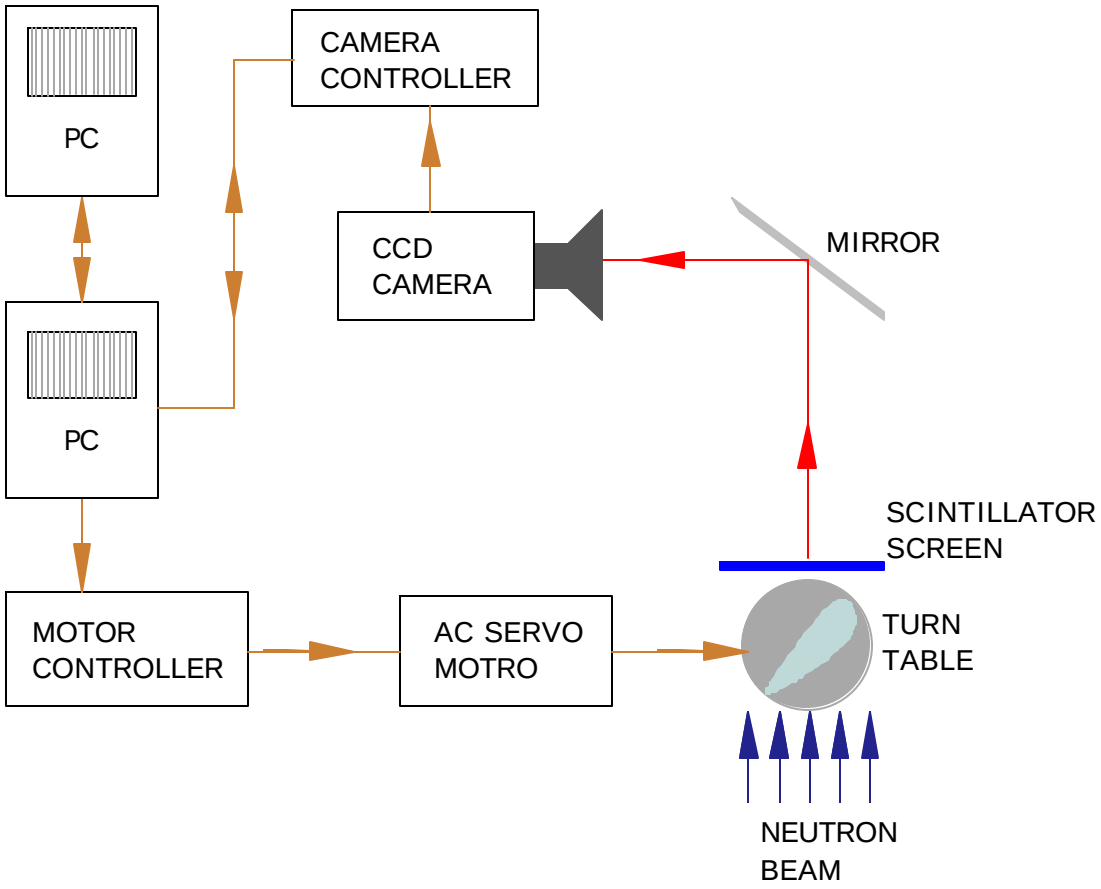

Figure 1: Tomography System

Photons generated in the screen are reflected from the mirror, pass through a lens and enter the CCD detector. A 50 mm lens provides an image pixel size of 0.057 cm while a 300 mm lens provides an image pixel size of 0.014 cm. The CCD detector has a rectangular array of 1024 x 1024 pixels (24 µm x 24 µm pixels). The quantum efficiency is highest in the 0.6-0.7 µm range where the scintillator emits its light[11].

The image data are collected in a 16-bit format. Image acquisition and reconstruction is controlled with two workstations. One provides control to the CCD camera and sample

turntable as well as image data capture functions. The other provides tomographic reconstruction and image analysis functions.

2. Preprocessing of Radiographs.

The characteristics of the radiographic images, used as projections for the tomographic reconstruction, set the fundamental limits on the accuracy of the reconstruction. The resolution limits and noise levels in the images along with processing to improve these characteristics are summarized in this section.

2.1 Spatial Resolution and Random Noise.

The size of detectable defects in tomographic reconstruction is limited by the spatial resolution of the initial radiographs. Placing cadmium squares 4 cm across and 0.076 cm thick at various distances in front of the scintillation screen determined the geometric sharpness of an edge. The resolution was calculated by fitting the general edge spread function[12] to a normalized intensity curve. With objects centered at 10 cm from the screen, resolutions of approximately 0.06 cm were found for the tomography system.

The sources of random noise in the beam signal include dark charge buildup in the CCD camera and fluctuation in the light intensity reaching the camera. The light intensity is affected by neutron beam fluctuations, the scintillation screen, lens system efficiency, etc. The random error was measured by dividing two images taken with the same exposure time and normalized to an average intensity of one. The fractional standard deviation in error signal reduced from 0.10 for a 0.16 s exposure to 0.01 for a 8.0 s exposure. Measurements indicate that about half of the noise is due to dark charge fluctuations that were seen to have linear time dependence. As shown in section 5, 100 ppm hydrogen in a 0.5 cm thick sample of titanium alloy causes a 0.005 relative change in intensity. To keep the noise fraction under 0.005, the two byte signal must be accumulated in less than 20 seconds. Longer exposures would decrease the beam noise, but this is offset by the increase in the dark charge noise. The optimum choice for random noise reduction would be an increase in beam flux.

2.2 Preprocessing of Images to Correct Systematic Noise Errors.

As a first step toward tomographic reconstruction, an accurate measure of the beam attenuation caused by an object is required. The objective is to find the intensity behind the object, I_o, normalized by the beam intensity, I_b, despite corruption due to system noise, image spreading, object scattering, and beam energy spread. An initial estimate can be found by only considering the dark charge intensity, I_d, the background noise, I_n, the object scattered beam intensity, I_s, and the fluctuation of the beam magnitude, f. The dark charge is subtracted during image acquisition. We shall consider the rest of the quantities to be spatially independent.

The intensity actually measured in an image without an object (the flat field image) is designated as I_{bf}.

$$I_{bf} = I_b + I_n. \tag{1}$$

Notice that I_n has been added to I_b thus including the effect of any light or neutrons scattered by the beam stop, etc. The noise signal, I_n, is found by placing a 2.5 cm thick strip of borated polyethylene on the beam side of the scintillation screen. The borated polyethylene effectively absorbs all neutrons incident on it so any intensity measured behind the strip is noise. The normalized intensity found behind the strip is 0.053.

The large size of the neutron backscatter and scattered light signals is a result of the large area of the beam. A small area beam would have much smaller scatter noise given the isotropic scattering of the neutrons and light. The advantage that size gives for fast processing of large objects adds an extra noise signal that must be removed.

Now consider images with objects. The intensity, I_{bo}, in an unobstructed pixel of an object image (i.e., no neutron absorption) is a function of several parameters, as follows,

$$I_{bo} = f\left(I_b + I_n + I_s\right) \tag{2}$$

where fluctuations of reactor power and object neutron scattering have been included as is. The intensity, I_{oo}, behind the object in an object image is

$$I_{oo} = f\left(I_o + I_n + I_s\right) \tag{3}$$

The intensity, I_{so}, behind the borated-poly strip in an object image is

$$I_{so} = f\left(I_n + I_s\right). \tag{4}$$

The neutron scattering detection method is similar to Ikeda, et al.[13]; however, they did not separate the background and object scatter signals. Other methods include Murata, et al.[14] We separate the signals since the object scatter signal changes with each image while the background scatter signal does not. The large mean free paths of neutrons coupled with large scattering cross sections leads to difficulties in physically preventing the scattered neutrons from reaching the scintillation screen. These problems are exacerbated by the fact that neutrons are mostly scattered and not absorbed by the objects being imaged. Additionally, the detection screen cannot be designed to absorb neutrons in only a narrow band of energies. In fact, the neutrons are scattered to lower energies where the screens are typically more sensitive. This is in contrast to the many techniques available for x-ray tomography[15].

Pixel by pixel division of the object image by the flat field image is equivalent to dividing equations (2) and (3) by I_{bf} and equation (4) by I_n. The result becomes the normalized image intensities in the unobstructed, behind the object, and behind the borated-polyethylene portions of a radiographic image:

$$d_{bof} = f\left(1 + d_n + d_s\right)/\left(1 + d_n\right) \tag{5}$$

$$d_{oof} = f\left(d_o + d_n + d_s\right) \tag{6}$$

and

$$d_{sof} = f\left(1 + d_s / d_n\right) \tag{7}$$

In these equations, the d are the signals normalized by the actual beam intensity, I_b, so d_o is I_o/I_b, dn is I_n/I_b, and d_s is I_s/I_b.

Solving for d_s using eq. (5)

$$d_s = \left(1 + d_n\right)d_{bof} / f - 1 - d_n. \tag{8}$$

Placing this into eq. (7) results in a solution for f in terms of d_{bof} and d_{sof}

$$f = \left(1 + d_n\right)d_{bof} - d_n d_{sof} \tag{9}$$

Given f and d_s, the object intensity normalized by the beam intensity, δ_o, becomes

$$d_o = \left(1 + d_n\right)d_{oof} / f - d_n - d_s \tag{10}$$

The procedure for determining d_o is:

1) Divide the object image by the flat field image.
2) Measure d_{bof} by averaging the intensity for a region of pixels that are not blocked by the scattering detector or by the object to be reconstructed.
3) Measure d_{sof} by averaging the intensity for a region of pixels that are located behind the scattering detector.
4) Calculate d_s from eq. (8) and f from eq. (9).
5) Calculate d_o for each pixel in the object image from eq. (10).

This procedure is repeated for each radiograph since beam magnitude variation, f, and object scattering, d_s, will change from image to image.

2.3 Beam Attenuation and Hardening.

The attenuation coefficient line integrals, $p(q,x,y)$, must be calculated for each pixel in the projection images. For a monoenergetic beam, exponential attenuation would be applicable.

$$p(q, x, y) = -\ln\left[I_o(q, x, y) / I_b(q, x, y)\right] \tag{11}$$

The neutron beam of the MNRC reactor is not monoenergetic. The spectrum has a Maxwellian distribution in the thermal region, a distribution proportional to 1/E above 0.5 eV, and a bump in the fast region around 2 MeV. Above 10 MeV, the distribution drops rapidly. In sample materials this leads to beam hardening. As the sample becomes thicker, the lower energy parts of the spectrum are depleted at a faster rate than the higher energy parts because of the larger cross section at low energy, decreasing the effective attenuation coefficient for thicker samples.

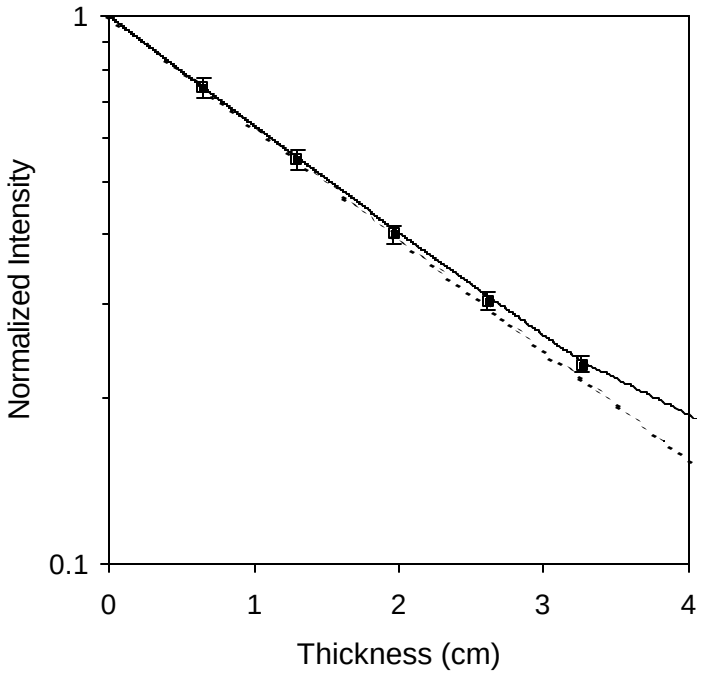

Figure 2: Dependence of the intensity on Ti6Al4V thickness. The solid curve is the fit to the data points represented by squares. The dashed curve is the result assuming exponential attenuation and a constant attenuation coefficient.

The correction for beam hardening in images is accomplished with a table of intensity versus titanium alloy thickness. The data in Table 1 is plotted in Figure 2 along with the exponential attenuation result. Table 1 was generated by measuring the neutron beam intensity as it passed through varying thicknesses of titanium. The standards of titanium alloy were obtained from the National Institute of Standards and Technology (SRM 654B, 3.5 cm diameter by 1.9 cm thick disks). The standards were certified to have less than 50 ppm hydrogen.

The table is filled by interpolation between the data points using the attenuation equation

$$\frac{I(T)}{I_o} = \int f(E)\exp(-m(E)T)(1-\exp(-p_d(E)))dE \qquad (12)$$

Here m is the attenuation coefficient, T is the sample thickness, and p_d is the line integral of the detector attenuation coefficient. The energy distribution, $f(E)$, of the beam has been characterized. The detector attenuation coefficient and the ratio between the thermal and epithermal parts of the beam energy spectrum can be optimized to provide a fit to the measured data. Eq. (12) does not replace the measured attenuation versus thickness data. It is simply an interpolating function that is more physically consistent than a linear, spline, or other function. The fit also provides the best approximation for extrapolation to thicknesses beyond those measured.

As in Phister, et al.,[16] it has been found empirically that the same correction applies to many different materials. This is reasonable since the metal constituents of these materials usually have cross section proportional to 1/E at low energy.

The preprocessing procedure for projection images is now complete. First, a flat field image and a dark charge image are taken. The object to be reconstructed is then placed on the turntable and the projection images are collected. The images are preprocessed to correct for noise errors resulting in images with intensities normalized to a maximum value of 1. Using the attenuation table, the intensities in each pixel are converted into equivalent thicknesses of the titanium alloy. The result of the tomographic reconstruction is a plot of the material attenuation coefficient relative to Ti6Al4V without error due to beam hardening.

3. The Hydrogen Attenuation Coefficient.

Estimates are now needed for the hydrogen signal relative to the titanium alloy signal. The attenuation caused by a number of test objects was measured. These plates and disks were placed so that a flat surface was presented to the beam for the purpose of attenuation measurements. The density of hydrogen, r_H, in the test objects was calibrated with gas fusion analysis and cold neutron prompt gamma activation analysis (CNPGAA)[17,18]. Using the table of Figure 1, the effective thickness, t_s, of the sample is found from the attenuation of the beam. The physical thickness, T, was also measured. The ratio of the hydrogen attenuation coefficient to the titanium alloy attenuation coefficient is given for each sample by

$$\frac{m_{100ppmH}}{m_{alloy}} = \frac{t_s - T}{T}\frac{100\,ppm}{r_H} \tag{13}$$

Here the attenuation coefficient has been scaled to 100 ppm, which is convenient for the embrittlement application. The average result for the test objects was that hydrogen at 100 ppm causes an increase in the normalized attenuation coefficient of 0.022 ± 0.0025. As seen in Table 1 the ratio holds over a wide range of hydrogen concentrations and alloy thicknesses. Note that this result is larger than the result derived from the thermal cross sections for the alloy elements (Ti 10.3 barns, Al 1.64 barns, V 9.88 barns) and 20.3 barns for unbound hydrogen.[19] Given the alloy density of 4.43 g/cm^3, the alloy attenuation coefficient is 0.546 cm^{-1}. The attenuation coefficient for 100 ppm hydrogen is 0.0053 cm^{-1}. The theoretical ratio is 0.0097, only half of the measured value. The measured ratio can be explained by the assumption that the hydrogen is not in a single atom, unbound state when diffused into the metal matrix of the alloy. For the case where molecules are of finite temperature, the cross section of hydrogen increases below 0.5 eV as the inverse of neutron energy, resulting in an average cross section of approximately 40 barns.[20,21]

4. Postprocessing of Reconstructions.

The spatial resolution and number of the initial projection images limit the size of detectable defects in tomographic reconstructions. For the detection of a low amount of

hydrogen in small or thin objects, postprocessing procedures become necessary. The procedure chosen is to align the reconstruction of an object being tested with a standard object.[22] The standard object is the same as the test object in composition and shape except the standard has little or no hydrogen. More than one object can be defined in an image, and the software aligns each object separately. After alignment, the standard object image is subtracted from the test object image. The result is an image that contains only the hydrogen signal plus any data noise. Any systematic errors such as reconstruction aliases should be removed. The procedure results in improved detection capability for the small hydrogen signal as well as data that can be more easily interpreted in an automated fashion.

Table 1: Attenuation coefficient of hydrogen relative to Ti6Al4V

Sample	Effective Thickness (cm)	Actual Thickness (cm)	ρ_H (ppm)	μ_{100}/μ_{alloy}
1	0.334	0.328	115	0.017
2	0.355	0.340	170	0.024
3	1.200	0.335	12900	0.020
4	1.710	0.344	17900	0.022
5	2.044	1.943	200	0.026
6	2.121	1.938	410	0.023
7	2.281	1.943	815	0.021
8	3.984	3.886	100	0.025
9	4.387	3.881	613	0.021
10	6.391	5.824	475	0.021
11	8.363	7.767	356	0.022

Consider the images resulting from the tomographic reconstruction of a test object and a standard object. The objects are assumed to be vertically aligned so only one 2-D slice is postprocessed at a time. The postprocessing algorithm creates object templates, aligns the objects' centers of mass, rotates the test object, generates a difference image, and reports the difference in attenuation coefficient. The first task is to determine the extent of objects in the images. Since we already know the effective attenuation coefficient of the object, we can set a cutoff value that is some fraction of the coefficient (usually 0.8). A template array is generated for each image by setting the value of pixels with attenuation coefficients above the cutoff to one, and the value of pixels with attenuation coefficient below the cutoff to zero. These template arrays delineate the pixels inside the objects. Of course, edge spread will limit the accuracy of determining which pixels are inside objects.

The test object image is then translated so that its center of mass is coincident with the center of mass for the standard object. Since the test object pixels are no longer at integer locations in the standard object coordinate system, the intensities are linearly weighted to the grid. After the test object has been translated, the test object template is updated.

Once the center of masses are coincident, the test object can be rotated to complete the alignment. For an object of unknown shape, a method is necessary to define its orientation. The ellipsoid of inertia provides the required information[23]. The angle of the principal axes with respect to the coordinate axes can be matched for the test and standard objects. It is assumed that the test and standard object orientations are within ±90° since the ellipse is symmetrical about its axes. Otherwise this spatial degeneracy could result in a 180° misalignment of the object orientations. This is not a problem since the objects and turntables are always started as close as possible to the same initial position. The orientation of the principal axis is found as follows. The moments and product of inertia (I_x, I_y, and I_{xy}) are determined at the center of mass for each object in the template images. The principal axes of inertia are then calculated.

Given these object orientations the test object can now be rotated to the same angle as the standard object. The rotation is centered at the center of mass. After rotation a new test object template, center of mass, and angle are calculated. These characteristics can be used to determine the effect of the linear weighting on the test object as well as the accuracy of the alignment.

The intensity values of the standard object images are subtracted from the intensity values of the test object image for each individual pixel. The result should be only the hydrogen signal except for data noise and edge spread artifacts. Edge artifacts could arise due to slight differences in the objects' shapes, linear weighting effects, variation in object orientation in the original projection images, etc. Since the attenuation coefficients drop off sharply at the edges, large spurious difference signals could occur. To reduce the chance for such spurious signals, the templates for the test image and the standard image are multiplied together. The difference image is then multiplied by the combined template. Pixels that are not included in both objects (test and standard) are removed from the resulting images.

By using the image comparison (subtraction) technique, we hope to preserve the surface signal as much as possible. Nonetheless, if hydrogen concentrates solely on the surface with no significant diffusion to thicknesses greater than a pixel width, we will have a significantly limited ability to achieve accurate detection. With the high diffusivity of hydrogen in metals, it is unlikely that only an extremely thin surface layer of hydrogen will be the normal condition; therefore, we are confident in the detection capability of our present method.

5. Results.

Reconstruction was accomplished with the filtered backprojection routine from the Donner algorithms library[24]. The exposure time for each projection images was 8.2 seconds. Another 13 seconds was required for downloading and dark charge subtraction by the PC. The reconstructions shown below were calculated from sets of 180 projections (one degree increments) resulting in an image acquisition time of 60 minutes. Preprocessing includes division by the flat field, correction for background, correction for reactor fluctuations, correction for scattering, and correction for beam hardening. This

section contains results from the reconstructions of NIST titanium standards, a phantom with various metals, and engine compressor blades. The reconstructions quantify the ability of the system with preprocessing to correctly report the titanium attenuation coefficient and the hydrogen concentration in calibrated samples. The response to metals with different attenuation coefficients indicates the ability to evaluate components made of various materials. The blade reconstructions show the result for thin objects.

The titanium alloy standards, previously used in the measurements of attenuation coefficient, were reconstructed. The standards are circular disks 3.5 cm in diameter and 1.97 cm thick. The axes of the disks were placed perpendicular to the rotation axis resulting in a rectangular cross section in the reconstruction. The samples had been degassed in vacuum and then placed into a sealed furnace system with a known volume of hydrogen.

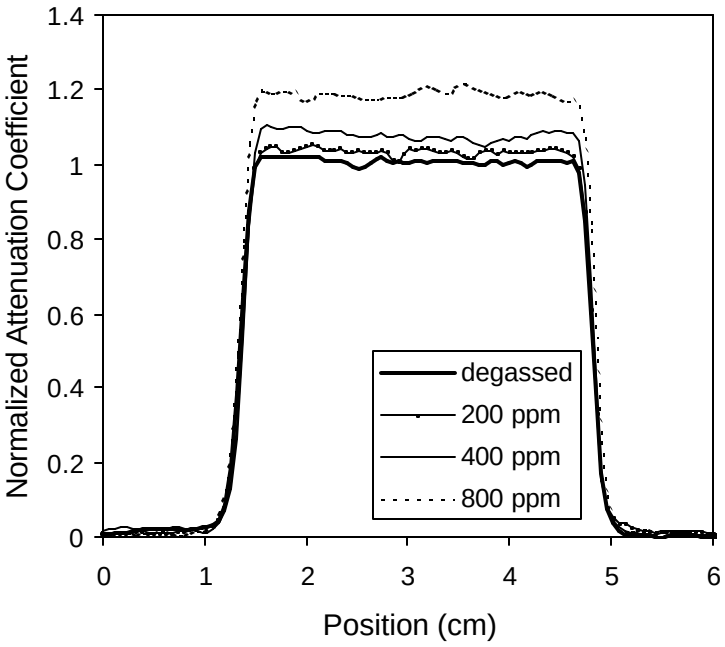

Figure 3: Cross section after reconstruction of the calibrated alloy samples having 0, 200, 400, and 800 ppm hydrogen.

Cross sections of the reconstructions are shown in Figure 3. As expected the degassed sample has a normalized attenuation coefficient near 1.0 with no systematic deviation from a flat profile. For this size sample there is no evidence of problems with beam hardening artifacts. The hydrogen appears to have diffused very uniformly into the other samples since the reconstructions do not indicate large gradients in the attenuation coefficient.

The results for hydrogen concentration are listed in Table 2. Concentrations were calculated from the volumetric uptake of hydrogen, from the change in weight of the samples, from CNPGAA, and from the average attenuation coefficient in a tomographic reconstruction. For comparison purposes, an average was taken across the reconstructions

since the other methods will only report the average hydrogen concentrations. The reported variation for the tomography results is the standard deviation of the attenuation coefficient from pixel to pixel. This could be the result of both system noise and actual hydrogen concentration variation. The neutron tomography result agrees to within 10% of the other methods for samples ranging from 200 ppm to 800 ppm hydrogen.

Table 2: Results of hydrogen detection in titanium alloy samples

Sample	volumetric estimate (ppm)	weight estimate (ppm)	CNPGAA estimate (ppm)	tomography estimate (ppm)
1	0	0	0 ± 6	21 ± 49
2	200	208	194 ± 35	159 ± 56
3	408	450	403 ± 56	356 ± 49
4	815	815	827	863 ± 48

More details concerning the hydrogen test standards can be found in reference 27.

6. Other Applications.

The tomography system has shown its capability to detect very small concentrations of hydrogen in a titanium matrix. In addition, the tomography system has been used to inspect o-rings in flight critical systems (Figure 4). The tomographic reconstruction shows the o-ring as it is located in the body of a one-inch thick stainless steel valve. Only materials with a certain range of attenuation coefficient are retained in the image. The result is removal of the valve leaving the o-ring visible for inspection. Note that a kink in the o-ring is easily observed in the image. Such defects could lead to valve malfunctions.

A further example of neutron tomographic inspection is shown in Figure 5. The ability of tomography to distinguish between various mineral deposits and glasses in rock has been of great interest to the UCD Geology Department researchers.

Figure 4: O-Ring

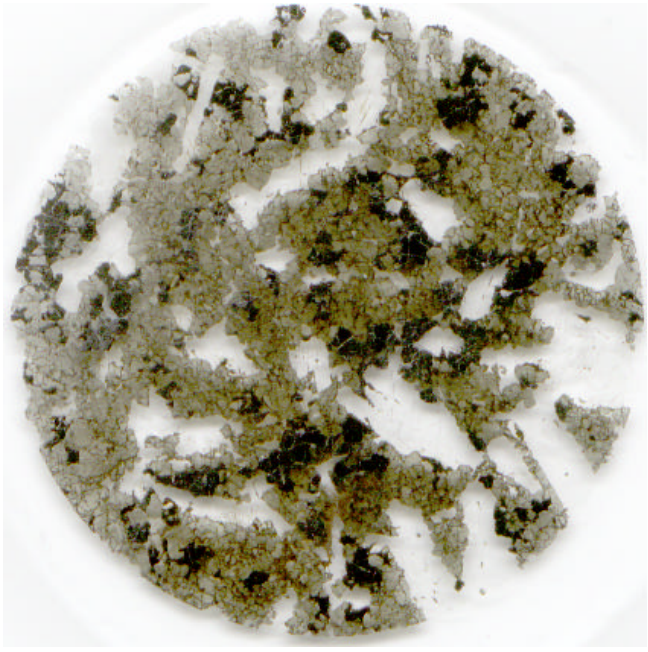

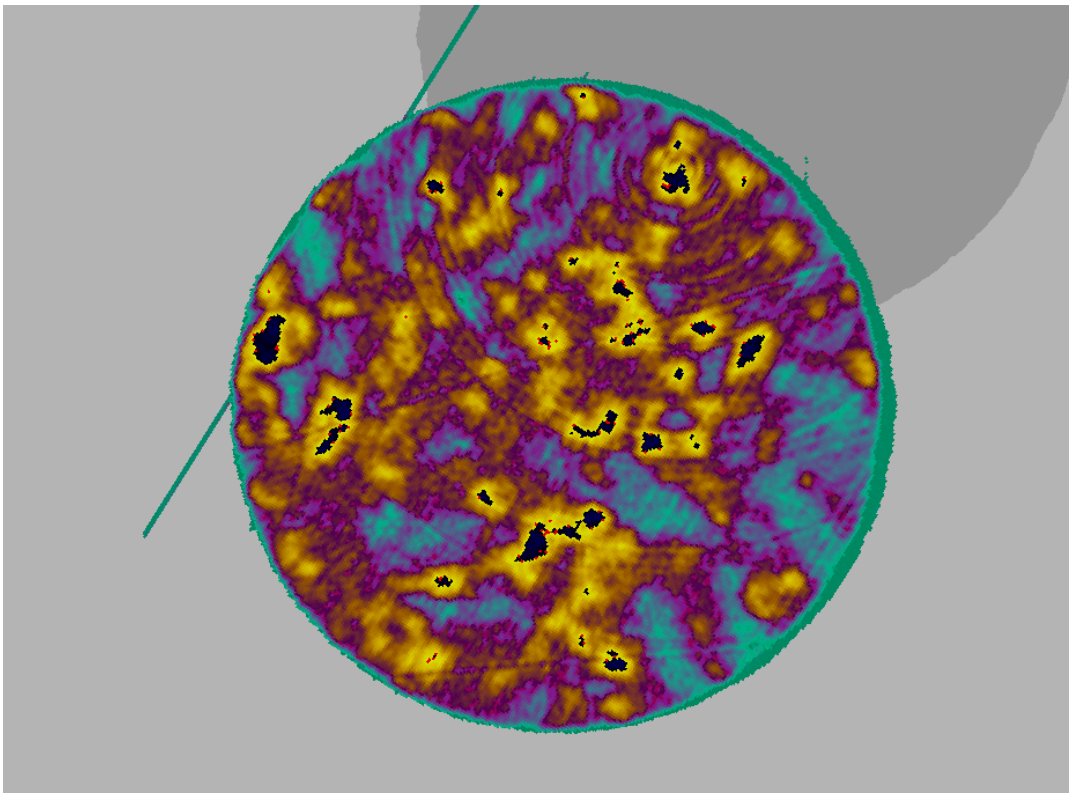

Figure 5A: Plane Polarized Light Image.
1) Section of drill core (~ 3 cm) from Skaergaard Intrusion, Greenland (perpendicular to Z axis).
2) Tomographic slice from same.

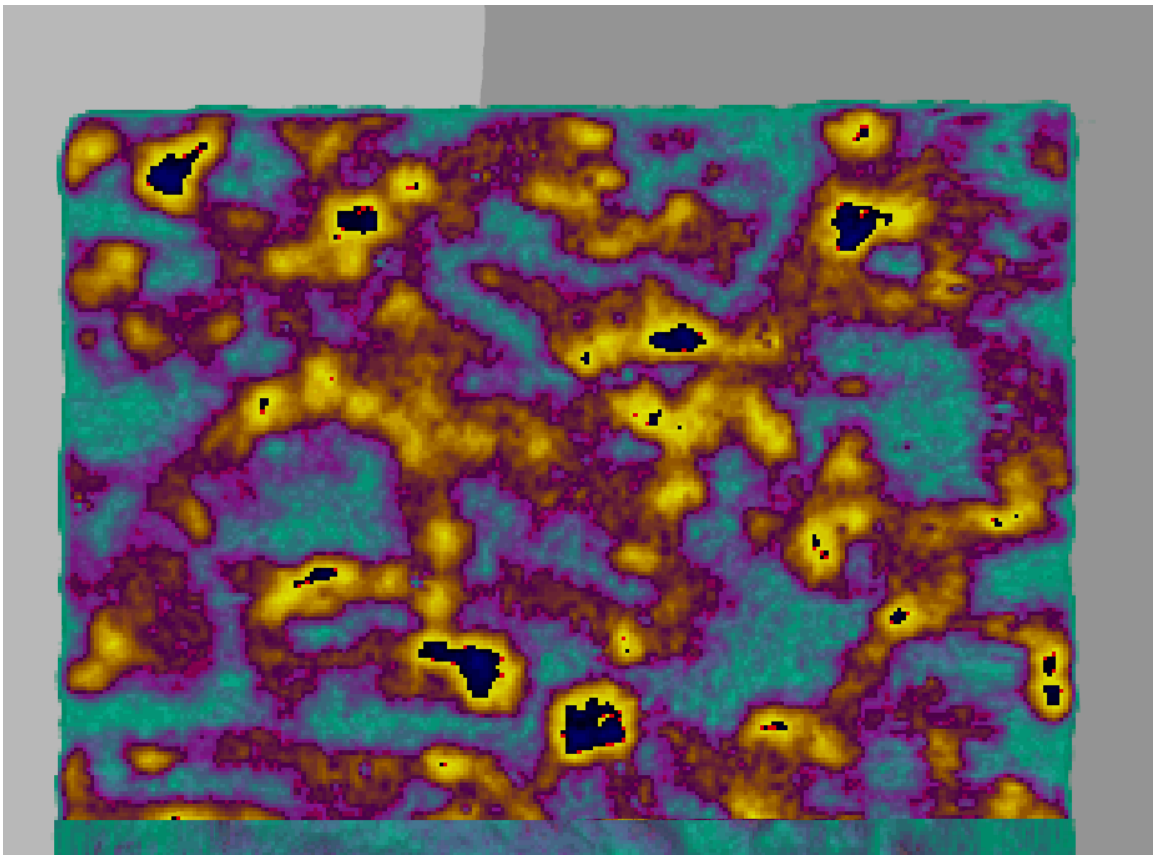

Figure 5 B: Parallel to Y direction.

7. Conclusion.

The UCD/MNRC neutron tomography system has demonstrated its versatility and capabilities over the last four years. In particular, the tomography system's ability to detect hydrogen in metal castings to levels below 200 ppm has been definitively demonstrated. The system is capable of attaining a spatial resolution of 0.057 mm with an acquisition time of 60 minutes. Preprocessing, to include CCD camera dark charge, and correction for background, reactor fluctuations, scattering and beam hardening was accomplished for each projection image. Comparison of standards without hydrogen to objects with hydrogen signals was used to detect the small hydrogen signals. The difference between the two reconstructed images reveals the hydrogen signal. The hydrogen determination results also agree with several other hydrogen detection methods. In addition to the hydrogen concentration work, the tomography system has also demonstrated its usefulness in inspection of o-rings and geological samples. The applications for neutron tomography continue to increase as advances in tomography software and hardware become available. Therefore, neutron tomography is becoming a more important inspection technique.

ACKNOWLEDGMENTS

The authors thank R.M. Linstrom, R.L. Paul, and M. Arif of the National Institute of Standards and Technology for the hydrogen loading of the various samples and the measurement of concentrations with CNPGAA.

REFERENCES

1. Froom, D.A., Barton, J.P., 1990. Aircraft neutron radiography – an overview. Neutron Radiography (3), 29-34, Kluwer Academic Publishers, and other articles in Part 13: Aerospace Applications.
2. Richards, W.J., 1990. Stationary neutron radiography system. Trans. Am. Nucl. Soc., 62, 142-143.
3. Alvar, K., Maung, T., Orphan, V., Polichar, R., 1990. Neutron radiography with SNRS. Neutron Radiography (3) 439-446, Kluwer Academic Publishers.
4. Patton, N.E., Williams, J.C., 1974. Effects of hydrogen on titanium and its alloys. Hydrogen in Metals, 409-432, American Society of Metals, Metals Park, OH.
5. Nelson, H.G., 1983. Hydrogen embrittlement. Treatise on Materials Science and Technology, 25, 275-359, Academic Press, New York, NY.
6. McFarland, E.W., Leigh, J., Lanza, R.C., 1995. Detection and characterization of the heterogeneous distribution of hydrogen in titanium compressor blades by neutron computed tomography. J. of Adv. Mater., 26 (3), 3-10.
7. Zanarini, M., Chirco, P., Rossi, M., Baldazzi, G., Guidi, G., Quersola, E., Scannavini, M.G., Casali, F., Garagnani, A., Festinesi, A., 1995. Evaluation of hydrogen content in metallic samples by neutron computed tomography. IEEE Trans. Nucl. Sci., 42 (4) 580-584.
8. Gibbons, M.R., Richards, W.J., Shields, K.C., 1996. Detection of hydrogen in titanium aircraft components using neutron tomography. Nondestructive Evaluation

of Aging Aircraft, Airports, and Aerospace Hardware, SPIE Proceedings, 2945, 104-115.
9. Private Communication, NE Technology, Inc., Monmouth Junction, NJ 08852.
10. Spowart, A.R., 1969. Measurement of the absolute scintillation efficiency of granular and glass neutron scintillators. Nucl. Inst. and Meth. A, 75, 35-42.
11. TE/CCD Detector Operation Manual and ST-138 Controller Operation Manual, 1993. Princeton Instruments, Inc., Trenton, NJ.
12. Harms, A.A., Wyman, D.R., 1986. Mathematics and physics of neutron radiography. D. Reidel Publishing Co., Dordrecht, Holland.
13. Ikeda, Y., Yokoi, M., Oda, M., Tamaki, M., Matsumoto, G., 1996. Correction of scattering neutron effects on neutron CT. Nucl. Inst. and Meth. A, 377, 85-89.
14. Murata, Y., Mochiki, K., Taguchi, A., Kobayashi, H., Turuno, A., Matubayashi, M., 1992. Two-dimensional neutron image excluding the effect of scattered neutrons. Neutron Radiography (4), 583-590, Gordon and Breach Sci. Pub.
15. Kak, A.C., Slaney, M., 1988. Principles of computerized tomographic imaging. IEEE Press, New York, NY.
16. Pfister, G., Gobel, J., Schatz, A.K., Siegel, C., 1992. A new method for the correction of beam hardening in fast neutron tomography. Neutron Radiography (4), 611-619, Gordon and Breach Sci. Pub.
17. Privett, M., 1994. Titanium/hydrogen panel standards. Letter from United Technologies Pratt & Witney, P.O. Box 109600, West Palm Beach, FL 33410.
18. Paul, R.L., Privett, M., Lindstrom, R.M., Richards, W.J., Greenberg, R.R., 1996. Analysis of hydrogen in titanium alloys by cold neutron prompt gamma activation analysis. Metall. Mater. Trans. A, 27A (11), 3682-3687.
19. Mughabghab, S.F., Divadeenan, M., Holden, N.E., 1981. Neutron cross sections, vol. 1. Academic Press, New York, NY.
20. Melkonian, E., 1949. Slow neutron velocity spectrometer studies of O_2, N_2, A, H_2, H_2O, and seven hydrocarbons. Physical Review, 76, 1750-1759.
21. Messiah, A.M.L., 1951. Scattering of slow neutrons by H2 and CH4. Physical Review, 84, 204-214.
22. Gibbons, M.R., Richards, W.J., Shields, K.C., 1999. Optimization of neutron tomography for rapid hydrogen concentration inspection of metal castings. Nucl. Inst. and Meth. A, 424, 53-57.
23. Goldstein, H., 1981. Classical mechanics. 198-203, Addison-Wesley, Reading, MA.
24. Heusman, R.H., Gullberg, G.R., Greenberg, W.L., Budinger, T.F., 1977. Donner algorithms for reconstruction tomography. Pub. 214, Lawrence Berkeley Laboratory, University of California, CA, October.
25. Ikeda, Y., Ando, A., Ohkubo, K., Yokoi, M., Kobayashi, H., 1990. A new imaging device for neutron CT. Neutron Radiography (3), 835-842, Kluwer Academic Pub.
26. Kobayashi, H., 1992. Recent development of cooled CCD camera for NR imaging tomography. Neutron Radiography (4), 553-560, Gordon and Breach Sci. Pub.
27. Richards, W.J., Gibbons, M.R., Shields, K.C., 2000. Advanced neutron tomography. SPIE Summer Meeting.